Mon. Not. R. Astron. Soc. **000**, 1–?? (2012) Printed 26 November 2012 (MN LaTeX style file v2.2)

arXiv:1211.5206v1 [astro-ph.SR] 22 Nov 2012

Competitive accretion in the protocluster G10.6-0.4?

Tie Liu[1]⋆, Yuefang Wu[1]†, Jingwen Wu[2], Sheng-Li Qin[3], Huawei Zhang[1].
[1] *Department of Astronomy, Peking University, 100871, Beijing China*
[2] *Jet Propulsion Laboratory, 4800 Oak Grove Dr., Pasadena, CA 91101, U.S.A*
[3] *I. Physikalisches Institut, Universität zu Köln, Zülpicher Str. 77, 50937 Köln, Germany*

26 November 2012

ABSTRACT

We present the results of high spatial resolution observations at 1.1 mm waveband, with the Submillimeter Array (SMA), towards the protocluster G10.6-0.4. The 1.1 mm continuum emission reveals seven dense cores, in which infall motions are all detected with the red-shifted absorption dips in HCN (3–2) line. This is the first time that infall is seen towards multiple sources in a protocluster. The dense core located in the center has the largest mass and mass infall rate and dominates the gas accretion of the protocluster, while the off-center cores have much smaller masses and mass infall rates, which favors the "competitive accretion" model. We also identified four infrared point sources in this region, which are most likely Class 0/I protostars. Two jet-like structures are also identified from Spitzer/IRAC image.

Key words: stars: formation — ISM: kinematics and dynamics — ISM: jets and outflows

1 INTRODUCTION

There are two most promising models to account for high-mass star formation (M >8 $M_\odot$). One is called the "monolithic collapse and disk accretion" (York & Sonnhalter 2002; McKee & Tan 2003), and the other is "competitive accretion" (Bonnell et al. 2002; Bonnell, Vine & Bate 2004; Bonnell & Bate 2006). The former one suggests that high-mass stars form directly from isolated massive gas clumps like low-mass star formation but with a much larger accretion rate. The latter claims that high-mass stars form in the center of a cluster through competitive gathering gas mass with the other off-center protostars.

The competitive accretion model was proposed based on the observational fact that most stars are formed in clusters, and most massive stars reside in the center, i.e, mass segregation (Bonnell et al. 2002). In this model, the mutual potential of the protostars in the cluster funnels gas down to the center, which results in higher gas densities and higher accretion rates for the few protostars located there. Thus the protostars located in the center can accrete more and more gas and form massive stars. However, till now, no convincing observational evidences support the "competitive accretion" model. What is the mass segregation in protoclusters? How do the protostars interact with each other? Do the protostars competitively accumulate masses under a common potential? To distinguish these two models, high spatial resolution observations towards protoclusters are critically needed.

Locating at a distance of 6 kpc, the dense clump G10.6-0.4 has been widely studied from centimeter to submillimeter wavelengths at various spatial resolutions (e.g., Liu, Zhang & Ho (2011) and the references therein). The previous centimeter observations have pointed out that a burst of massive star formation in its central region (Ho, Klein & Haschick 1986; Keto, Ho & Haschick 1987, 1988; Sollins et al. 2005). A flatten rotating torus is found in the central parsec region of the dense clump (Ho & Haschick 1986; Liu et al. 2010a). Gas infalling was also revealed in the form of redshifted absorption seen against the continuum source (Keto, Ho & Haschick 1987, 1988; Sollins et al. 2005). Multiple outflows were detected in the ^{12}CO (2–1) and HCN (3–2) lines (Liu, Ho & Zhang 2010b). All the previous observations indicate a high-mass star cluster is forming in a dense clump (Liu, Zhang & Ho 2011). Thus it is a good target for testing different models for high mass star foramtion with sufficiently high spatial resolution observations and sensitive molecular tracers for infall motion. In previous VLA observations (Keto, Ho & Haschick 1987, 1988; Sollins et al. 2005), the NH_3 lines used as a tracer for infall motions only revealed the gas flow in the inner warm part near the central ultracompact HII region, which cannot provide information of the infall motions in the other less dense and colder parts of the dense clump. In this paper, with the HCN (3–2) line, which is a good tracer for infall motions (Liu et al. 2011a,b; Wu & Evans 2003), we can reveal the pattern of infall motions in the whole dense clump

---

⋆ E-mail: liutiepku@gmail.com
† E-mail: yfwu.pku@gmail.com

and uncover the accretion mode for the formation of a high-mass star cluster.

2 OBSERVATIONS

The observations of G10.6+0.4 were carried out with the SMA in July 2005 with seven antennas in its compact configuration and in September 2005 with six antennas in its extended configuration. The phase reference center of both observations was R.A.(J2000) = $18^{h}10^{m}28.698^{s}$ and DEC.(J2000) = -19°55′48.68″. The 345 GHz receivers were tuned to 265 GHz for the lower sideband (LSB) and 275 GHz for the upper sideband (USB). The frequency spacing across the spectral band is 0.8125 MHz or ∼1 km s^{-1} for both configurations.

In both configuration observations, Jupiter, Uranus and QSO 3c454.3 were observed for antenna-based bandpass correction. QSOs 1741-038 and 1908-201 were employed for antenna-based gain correction. Uranus was observed for flux-density calibration.

Miriad was employed for calibration and imaging (Sault, Teuben & Wright 1995). The 1.1 mm continuum data were acquired by averaging all the line-free channels over both the 2 GHz of upper and lower spectral bands. MIRIAD task "selfcal" was employed to perform self-calibration on the continuum data. The gain solutions from the self-calibration were applied to the line data.

The synthesized beam size and 1 σ rms of the dust emission observed in the compact configuration is $3''.47 \times 2''.89$ (PA=-45.7°) and 30 mJy beam^{-1}, respectively. The continuum data combined from both configurations yield a synthesized beam of $1''.24 \times 1''.11$, P.A.=-61°.6, and 1 σ rms of 10 mJy beam^{-1} in the uniform weighted map.

IRAC data were also retrieved from the database of GLIMPSE.

3 RESULTS

3.1 1.1 mm continuum emission

The 1.1 mm continuum image obtained from the SMA compact array is shown in red solid contours in the upper panel of Figure 1. Despite of the central elongated clump, two small lumps were found in the north-east and north-west. The two UC HII regions identified by Liu, Ho & Zhang (2010b) were denoted as black plus symbols. The emission peak of the 1.1 mm continuum emission coincides with the central bright UC HII region. The deconvolved size of the large clump is $3''.67 \times 1''.07$ (P.A.=-64.1°). By combining the data of the compact and extended configurations of SMA, we obtained a much higher spatial resolution ($1''.24 \times 1''.11$, P.A.=-61°.6) image of the 1.1 mm dust continuum emission. As shown in the lower panel of Figure 1, The large clump detected by the compact array is further resolved into seven dense cores, which are denoted from "A" to "G". The positions, integrated intensity and radii of these cores are listed in columns 2-4 of Table 1.

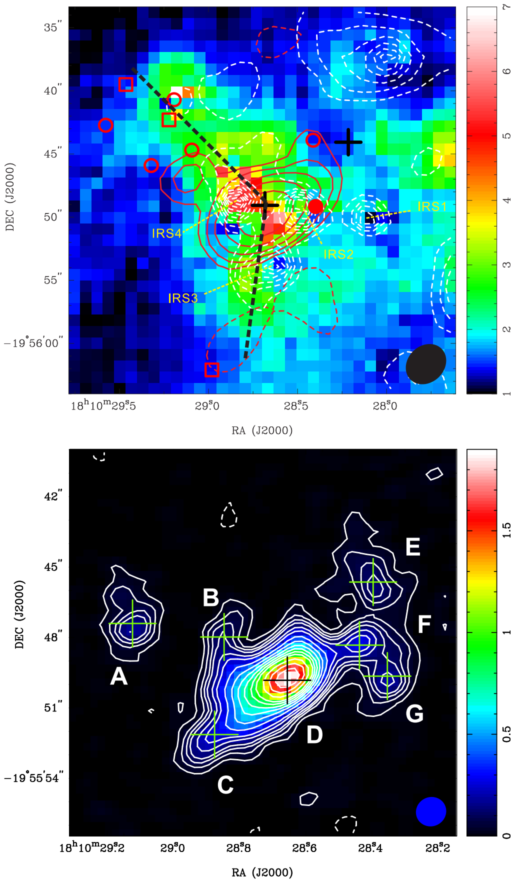

Figure 1. Upper: The flux ratio map of [4.5]/[3.6] is shown in color scale. The white dashed contours represent the distribution of 8 μm emission. The contour levels are from 400 to 1200 mJy/sr in a step of 100 mJy/sr. The 1.1 mm continuum from the compact configuration is shown as red solid contours. The contour levels are (-5,5,10,20,40,80,160)×0.03 Jy/beam (1 σ). The two black plus symbols mark the positions of the UC HII region. The red open circles and open boxes mark the locations of the blueshifted and redshifted ^{12}CO outflow interaction signatures (Liu, Ho & Zhang 2010b). The red solid circle is the location of the HCN (3–2) outflow. The names of the four infrared point sources are labeled as IRS1-4. The two dashed long lines denote the directions of finger-like structures. Lower: The 1.1 mm continuum from combining the compact and extended configurations is shown in white solid contours and in color scale. The contour levels are (-3,3,6,9,12,18,24,36,48,60,72,84,96,120,144,168)×0.01 Jy beam^{-1} (1 σ). The positions of the cores are marked with "crosses" and their names are labeled from "A" to "G".

Assuming that the dust emission is optically thin and the dust temperature equals the rotational temperature (87 K) of $CH_3^{13}CN$ (Beltrán et al. 2011), the masses of seven cores can be obtained with the formula $M = S_\nu D^2/\kappa_\nu B_\nu(T_d)$, where S_ν is the flux of the dust emission at 1.1 mm, D is the distance, and $B_\nu(T_d)$ is the Planck function. The dust opacity $\kappa_\nu = \kappa_{1300}(\frac{1300\mu\mathrm{m}}{\lambda})^{\beta}$=0.011, where β=1.5 is the dust opacity index and $\kappa_{1300} = 0.009\mathrm{cm}^2\mathrm{g}^{-1}$ is the dust opacity at 1300 μm derived from a gas/dust model with thin ice mantles (Ossenkopf & Henning 1994). Here the ratio of gas to dust is taken as 100. Since the central core (D) is a UC HII region, which should have a higher temperature than the clump averaged temperature derived from $CH_3^{13}CN$ lines, we also derived a lower limit for the mass and volume density for it by assuming a dust temperature of 200 K. The inferred masses and volume density of these

Table 1. Parameters of each dense core.

Name	Offset ($''$,$''$)	S_ν (Jy)	R (10^3 AU)	n (10^7 cm^{-3})	M ($M_\odot$)	V_{lsr} (km s^{-1})	σ_{NT} (km s^{-1})
A	(6.0,1.3)	0.37(0.06)	4.3(0.5)	1.2(0.5)	31(5)	-7.50(0.06)	1.72(0.06)
B	(2.1,0.7)	0.23(0.03)	2.7(0.3)	3.1(1.1)	19(2)	-3.73(0.23)	1.80(0.20)
C	(2.5,-3.5)	0.56(0.03)	3.5(0.2)	3.3(0.6)	46(2)	-5.10(0.07)	1.43(0.07)
D	(-0.3,-1.2)	4.81(0.31)^a	6.0(0.3)	[2.5,5.9]	[165,400]	-2.74(0.05)	2.22(0.04)
E	(-4.3,3.0)	0.50(0.07)	6.4(0.8)	0.6(0.2)	41(6)	-0.07(0.14)	3.13(0.13)
F	(-3.7,0.4)	0.60(0.07)	3.7(0.4)	3.1(1.1)	50(6)	-1.07(0.11)	2.29(0.11)
G	(-4.9,-1.0)	0.37(0.04)	3.5(0.3)	2.4(0.7)	31(3)	-2.35(0.15)	1.92(0.13)

[a] Since the integrated flux density at 1.3 cm is as high as 2.5 Jy (Sollins et al. 2005), the free-free contribution to the 1.1 mm can't be ignored. Assuming optically thin free-free emission ($S_\nu \propto \nu^{-0.1}$) (Beltrán et al. 2011), 1.99 Jy of free-free emission was subtracted from the total flux 6.8 Jy.

cores are listed in columns 5 and 6 of Table 1. The masses of the cores range from 19 to 165/400 $M_\odot$.

3.2 Infrared emission

Four infrared point sources locating at the central part are revealed by the 8 µm emission presented as white dashed contours in the upper panel of Figure 1, which are denoted as IRS1-4. IRS1 locates west and is not associated with the 1.1 mm dust emission. The other three infrared point sources form a triangular system, whose geometric center coincides with the 1.1 mm emission peak. All the four infrared point sources have colors [3.6]-[4.5]⩾0.4 and [5.8]-[8.0]⩾1.1, indicating they are most likely protostars (Class 0/I objects) (Qiu et al. 2008).

The flux ratio map of [4.5] to [3.6] µm emission is shown in color scale in the upper panel of Figure 1. Two finger-like structures are revealed and marked by the two long dashed lines. Despite of the finger-like structures, two red spots with ratios larger than 4 are found near the 1.1 mm emission peak. The flux ratio of [4.5] to [3.6] in the jets is comparable or higher than ~1.5 in contrast to the stars (Takami et al. 2010). The two finger-like structures may depict the jets generated from the protocluster G10.6-0.4. The roots of the two "fingers" connect with two red spots, indicating the interaction between the shocked jets and the envelope. We also noticed that the ^{12}CO outflow knots distribute along the finger-like structures and mainly locate at the outer layer or the tip of the jets, indicating the ^{12}CO outflow gas is entrained and accelerated by the collimated jets.

3.3 Line emission

The source averaged HCN (3–2) and CH_3OH ($5_{2,3}$-$4_{1,3}$) lines are shown in Figure 2. As shown in the last panel, the HCN (3–2) line averaged over the whole clump has an inverse P-cygni profile, indicating that the whole protocluster is in overall collapse. As marked by the red dashed lines, red-shifted absorption dips were detected in the HCN (3–2) line, indicating gas infalling is taking place towards these dense cores. This is the first time that infall is seen towards multiple sources in a protocluster. Only core "F" and core "G" show strong high velocity blue wings, suggesting that the previous discovered HCN outflow (Liu, Ho & Zhang 2010b) in this region is driven by the forming protostars in core "F" and core "G". The CH_3OH ($5_{2,3}$-$4_{1,3}$) line is single-peaked towards all the cores. The systemic velocities of the CH_3OH ($5_{2,3}$-$4_{1,3}$) line are listed in column 7 of Table 1. We found the CH_3OH ($5_{2,3}$-$4_{1,3}$) line is red-shifted towards the western cores ("E", "F", and "G") and blue-shifted towards the eastern cores ("A", "B", and "C").

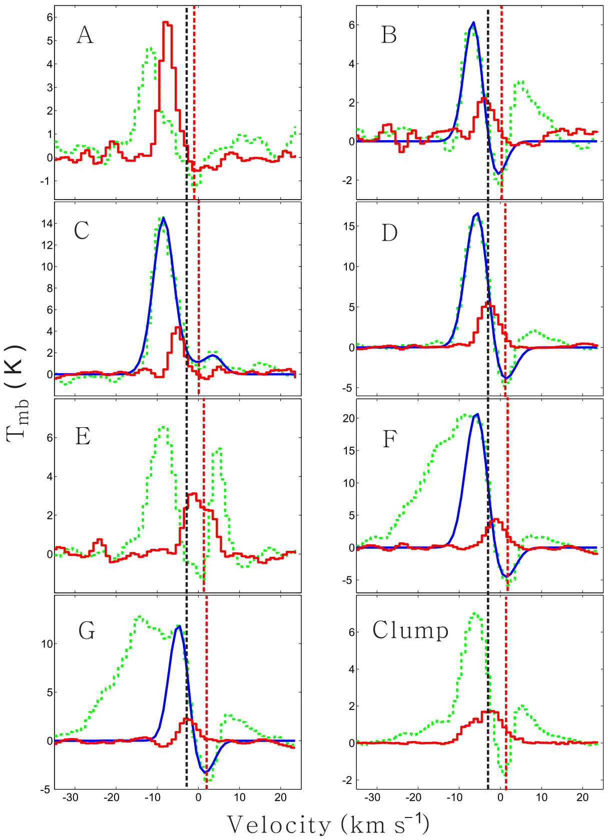

Figure 2. Spectra averaged over each core. green: HCN (3–2), red: CH_3OH ($5_{2,3}$–$4_{1,3}$). The last panel presents the clump averaged spectra obtained only from compact configuration. The black dashed lines mark the position (-3 km s^{-1}) of the systemic velocity. The red dashed lines mark the absorption dips. The best "two-layer" model fits towards the dense cores are exhibited as blue solid lines.

Table 2. Best fitting results for the HCN (3–2) line with the enhanced two layer models

Name	τ_0	f	J_c (K)	J_f (K)	J_r (K)	V_{lsr} (km s^{-1})	σ (km s^{-1})	V_{in} (km s^{-1})	$\dot{M}_{obs}$ (10^{-2} $M_\odot \cdot yr^{-1}$)	$\dot{M}_{BH}$ (10^{-2} $M_\odot \cdot yr^{-1}$)
B	0.5	0.4	49.3	8.1	38.7	-3.9	2.5	1.5	0.7(0.3)	0.5(0.3)
C	2.8	0.5	54.8	25.2	51.0	-2.3	3.6	1.6	1.3(0.3)	6.3(1.6)
D	0.5	0.4	91.3	22.8	70.8	-2.5	2.7	2.8	[4.9,11.9]	[16.0,243.2]
F	0.7	0.3	65.9	8.1	63.6	-2.5	2.7	2.7	2.3(1.0)	1.8(0.8)
G	1.1	0.4	44.6	11.4	32.0	-1.6	2.3	2.5	1.4(0.5)	0.9(0.4)

4 DISCUSSION

4.1 Gas inflow in the protocluster G10.6-0.4

The redshifted absorption in the HCN (3–2) line indicate gas infalling towards the cores (Welch et al. 1987). Interferometers can resolve out the extended emission and create kind of artifacts that may appear like absorption features, especially close to the line center. However, the absorption dips in the HCN (3–2) line are redshifted by several km s^{-1} from the systemic velocity, which should not be caused by the missing flux. Especially, the HCN (3–2) line towards core D, F and G shows clearly inverse P-cygni profiles with the absorption dips ∼5 K (∼ 5σ) below the continuum, indicating gas infalling towards the bright continuum background (Welch et al. 1987).

To investigate the properties of the absorbing gas, the profiles of the HCN (3–2) line were modeled with an enhanced version of the "two-layer" method (Myers et al. 1996; Di Francesco et al. 2002). In that model, a continuum source is located in between the two layers. Each layer has peak optical depth τ_0, velocity dispersion σ, and approach speed V_{in}. The line brightness temperature at velocity V is (Di Francesco et al. 2002):

$$\Delta T_B = (J_f - J_{cr})[1 - exp(-\tau_f)] + (1-\Phi)(J_r - J_b) \\ \times[1 - exp(-\tau_r - \tau_f)]$$

where

$$J_{cr} = \Phi J_c + (1-\Phi)J_r$$

and

$$\tau_f = \tau_0 exp[\frac{-(V - V_{in} - V_{LSR})^2}{2\sigma^2}]$$

$$\tau_r = \tau_0 exp[\frac{-(V + V_{in} - V_{LSR})^2}{2\sigma^2}]$$

J_c, J_f, J_r, J_b are the Planck temperatures of the continuum source, the "front" layer, the "rear" layer and the cosmic background radiation, respectively. $J = \frac{h\nu}{k}\frac{1}{exp(T_0/T)-1}$ is related to the blackbody temperature T at frequency ν, where h is Planck's constant, and k is Boltzmann's constant (Myers et al. 1996). Φ is the filling factor of the continuum source. We did not take outflow into the modeling. The lines towards core A and core E were not modeled because they seem to be greatly affected by the missing flux. The best fits are displayed in Figure 2 and the parameters of the best fits are summarized in Table 2.

The kinematic mass infall rate can be calculated using $dM/dt=4\pi n\mu_G m_{H_2} R_{in}^2 V_{in}$, where V_{in} is the infall velocity, $\mu_G = 1.36$ and m_{H_2} are the infall velocity, the mean molecular weight, and the H_2 mass, respectively. The radius and volume density of the cores are taken as infall radius R_{in} and volume density n in the calculation. The derived mass infall rates are listed in the tenth column of Table 2.

The "competitive accretion" model predicts the accretion rates in the virialized cluster are primarily determined by the Bondi-Hoyle type accretion rates (Bonnell et al. 2002; Bonnell & Bate 2006). However, this argument was often doubted and criticized by people (Krumholz, McKee & Klein 2005). The Bondi-Hoyle type accretion rates are believed too low to significantly increase the protostars' masses due to large velocity dispersion in turbulent cores (Krumholz, McKee & Klein 2005). And the radiative feedback from the massive protostars may also prevent Bondi-Hoyle accretions in the cluster (Edgar & Clarke 2004). Does the mass accretion in G10.6-0.4 favor the Bondi-Hoyle type accretion? The Bondi-Hoyle accretion rates of the dense cores in G10.6-0.4 are calculated as (Krumholz, McKee & Klein 2005):

$$\dot{M}_{BH} \approx 4\pi\rho\frac{(GM)^2}{(\sqrt{3}\sigma)^3} \qquad (1)$$

where G is the Gravitational constant, ρ and M are the mean density and mass of the dense cores, respectively. The one dimensional velocity dispersion $\sigma = \sqrt{\sigma_{NT}^2 + \sigma_{Therm}^2}$. The one dimensional thermal velocity dispersion $\sigma_{Therm} = \sqrt{\frac{kT_k}{m_{H_2}\mu}}$=0.51 km s^{-1}, where μ = 1.36 and T_k=87 K. The one dimensional non-thermal velocity dispersion listed in the last column of Table 1 is estimated from the CH_3OH ($5_{2,3}$-$4_{1,3}$) line through $\sigma_{NT} = \sqrt{\sigma_{CH_3OH}^2 - \frac{kT_k}{m_{CH_3OH}}}$. The calculated Bondi-Hoyle accretion rates are listed in the last column of Table 2. One can find except core "C" and core "D", the Bondi-Hoyle accretion rates of the other cores are similar to the observed mass infall rates, indicating the accretion in them is Bondi-Hoyle type. The Bondi-Hoyle accretion rates in core "C" and core "D" are significantly larger than their observed mass infall rates, indicating the accretion there is greatly resisted by the feedback from the massive protostars located in the center. However, the central massive core has accumulated enough mass to maintain a large accretion rate. With the present observations, we are unable to estimate how many accreted gas by the dense cores falls onto the protostars. But the central massive protostars seem to continue growing mass by accreting ionized gas passing through the ionization boundary of the ultracompact HII region (Keto 2002).

4.2 Competitive accretion in G10.6-0.4?

From Figure 2, one can find the absorption dips of the HCN (3–2) line are at nearly the same velocity, indicating the gas infalling towards these cores is dominated by a common potential. In free fall case, the effective infall radius r_{in} of the central dense core only due to gravity can be estimated by use of:

$$r_{in} = \frac{2GM}{V_{in}^2} \tag{2}$$

The estimated r_{in} is ~36000 — 87000 AU, which is much larger than the clump size (~10000 AU), indicating that the central dense core dominates the gravity of the clump and thus can competitively gather gas mass with the other off-center protostars from the gas reservoir of the clump. From Table 1 and 2, one can find that the central dense core (core "D") has the largest mass and mass infall rate, but the surrounding smaller cores have much smaller mass and mass infall rate, indicating that the mutual potential of the protocluster likely funnels gas down to the center. This picture favors the "competitive accretion" model.

The difference between the "competitive accretion" model and the "monolithic collapse and disk accretion" lies primarily in how and when the mass is gathered to form the massive star (Bonnel 2008). Does it occur in the pre-stellar stage due to turbulence, or does it occur subsequently due to accretion in a common potential (Bonnel 2008). G10.6-0.4 is a much evolved protocluster. But the protostars and their gas reservoirs (dense cores) in G10.6-0.4 are still accumulating masses from the gas reservoir of the clump, indicating that the cores in G10.6-0.4 are most likely formed due to accretion rather than pre-existing.

At the present time, we can not make unambivalent conclusion that the protocluster in G10.6-0.4 is formed through competitive accretion due to uncertainties in estimating the masses and mass infall rates. However, we clearly revealed the mass segregation in this region and the cores seem to still accumulate masses due to a common potential. Further higher sensitivity and resolution observations especially from the ALMA can give a more thorough understanding of the situations in this region especially of the interaction among the individual cores.

ACKNOWLEDGMENTS

We are grateful to the SMA staff. This work was funded by China Ministry of Science and Technology under State Key Development Program for Basic Research 2012CB821800 and the NSFC grant 11073003.

REFERENCES

Di Francesco, J., Myers, P. C., Wilner, D. J., Ohashi, N., Mardones, D., 2001, ApJ, 562, 770

Edgar, R., & Clarke, C., 2004, MNRAS, 349, 678

Beltrán, M. T., Cesaroni, R., Neri, R., & Codella, C., 2011, A&A, 525, 151

Bonnell, I. A., Bate, M. R., Clarke, C. J., Pringle, J. E., 2002, MNRAS, 323, 785

Bonnell, I. A., Vine, S. G., & Bate, M. R., 2004, MNRAS, 349, 735

Bonnell, I. A. & Bate, M. R., 2006, MNRAS, 370, 488

Bonnell, I. A., 2008, ASPC, 390, 26

Ho, P. T. P., & Haschick, A. D., 1986, ApJ, 304, 501

Ho, P. T. P., Klein, R. I., & Haschick, A. D., 1986, ApJ, 305, 714

Keto, E. R., Ho, P. T. P., Haschick, A. D., 1987, ApJ, 318, 712

Keto, E. R., Ho, P. T. P., Haschick, A. D., 1988, ApJ, 324, 920

Keto, E., 2002, ApJ, 568, 754

Krumholz, M. R., McKee, C. F., & Klein, R. I., 2005, Nature, 438, 332

Liu, H. B., Ho, P. T. P., Zhang, Q., Keto, E., Wu, J., Li, H., 2010a, ApJ, 722, 262

Liu, H. B., Ho, P. T. P., & Zhang, Q., 2010b, ApJ, 725, 2190

Liu, H. B., Zhang, Q., & Ho, P. T. P., 2011, ApJ, 729, 100

Liu, T. Wu, Y., Zhang, Q., Ren, Z., Guan, X., Zhu, M., 2011a, ApJ, 728, 91

Liu, T., Wu, Y., Liu, S.-Y., Qin, S.-L., Su, Y.-N., Chen, H.-R., Ren, Z., 2011b, ApJ, 730, 102

McKee, C. F., & Tan, J. C., 2003, ApJ, 585, 850

Myers, P. C., Mardones, D., Tafalla, M., Williams, J. P., & Wilner, D. J. 1996, ApJ, 465, L133

Ossenkopf, V., & Henning, T. 1994, ApJ, 291, 943

Qiu, K., Zhang, Q., Megeath, S. T., Gutermuth, Robert A., Beuther, H., et al., 2008, ApJ, 685, 1005

Sault, R. J., Teuben, P. J., & Wright, M. C. H., 1995, in ASP Conf. Ser. 77, Astronomical Data Analysis Software and Systems IV, ed. R. A. Shaw, H. E. Payne, & J. J. E. Hayes (San Francisco, CA: ASP), 433

Sollins, P. K., Zhang, Q., Keto, E., Ho, P. T. P., 2005, ApJ, 624, L49

Takami et al., 2010, ApJ, 720, 155

Welch, Wm. J., Dreher, J. W., Jackson, J. M., Terebey, S., Vogel, S. N., 1987, Science, 238, 1550

Wu, Jingwen., & Evans, Neal J., II., 2003, ApJ, 592, L79

Yorke, H. W. & Sonnhalter, C., 2002, ApJ, 569, 846.